A detail computational hydro - acoustics analysis for hydrofoils with straight and wavy leading edges

Nicolas Charalambous, Ian Eames[1]

[1]Department of Mechanical Engineering, University College London (UCL), WC1E 7JE, UK.

ABSTRACT

In this paper, we examine the influence of wavy leading edges (WLE) of a lifting surface on the mechanism of cavitation formation and noise generation. The results of two NACA 63_4-021 hydrofoils with different wavy leading edges are compared with a NACA 63_4-021 hydrofoil with a straight profile under different operational conditions. This problem is studied numerically using an unsteady RANS solver with a multiphase mixture flow model. The results are contrasted against a hydrofoil with a straight leading edge. The CFD method applied for solving the incompressible hydrodynamic code is combined with the Schnerr-Sauer cavitation model and with the Ffowcs-Williams Hawking (FW-H) integral formulation that can solve the hydro-acoustics problem. Furthermore, the spherical wave equation is applied in order to capture the monopole contribution of the cavitation volume fluctuations. The leading wavy edge leads to the generation of streamwise vorticity which causes the attached wake to become unstable leading to a smaller cavitation formations resulting to reduced pressure noise.

Keywords

Cavitation, Monopole noise, Cavitation noise, FW-H formulation, tubercles.

1 INTRODUCTION

The International Maritime Organization (IMO) recognized the studies proving the adverse effect of underwater noise to the marine environment and more specific to marine mammals and in 2014 decided to develop Guidelines (Guidelines for the reduction of underwater noise from commercial shipping to address impacts on marine life) aiming at the reduction of underwater noise from commercial shipping.

A primary agent for underwater noise is due to cavitation. Cavitation noise is an extremely challenging area of engineering because its spans a wide range of length and timescales. Cavitation noise is generated by the rapid collapse and growth on vapour and gas bubbles within water. Cavitation is initiated at microscopic nucleation points which collectively influence the macroscopic flow around propellers. The velocity of bubble collapse or oscillation, and the speed of sound propagation tend to be much faster than the flow speed. Presently, CFD is the only available tool to understand the coupled physics of cavitation and sound generation.

Cavitation tends to occur mainly on the propellers since they move rapidly relative to the local water column, leading to pressures low enough to initiate cavitation. Due to the steep angle of incidence of propeller blades, relative to the incident flow, low pressure regions tend to occur near to the leading edge of the hydrofoils and propeller blades. In this paper, we explore the effect of modifying the geometry of the leading edge to influence the generation of cavitation bubbles and the stability. The advantages of the foils with protuberances have been studied both computationally and experimentally in the absence of cavitation and have attracted the interest of many researchers due to their ability to sustain Lift at high angles of attack without a drastically increase of Drag and therefore they can be considered as effective control flow devices.

Miklosovic et al. (2004), Johari (2007) and Custodio (2008) have identified in their research that the interference of the vorticity strength is causing the momentum exchange in the boundary layer and therefore prolonging the flow attachment to the surface of the foil.

Custodio (2008) studied experimentally sinusoidal hydrofoils of different amplitude and wavelength observing the advantage of these hydrofoils in high angles of attacks and in the post-stall regions where the lift is generated due to vortices caused by the presence of the protuberances. The generation of these vortices and the interaction with the boundary layer of the hydrofoil need to be further studied in cases for cavitation. For a low Reynolds number cases Hansen et al. (2017) studied experimentally and computationally the streamwise vorticity distribution, that is generated by the strong pressure gradients present in the leading edge causing the increase of vorticity in this region. The vorticity is stretched, tilted and diffused in three dimensions, these processes can lead to the generation of a pairs of streamwise vortices that are present in each one of the tubercle peaks. For high angle of attack it was found that

the separation zone that is present downstream the tubercles forms a horseshoe shape and the zone is bounded by a canopy boundary layer vorticity that results to the increase of circulation of the primary streamwise vortices that are generated by the tubercles and are extended to the streamwise direction.

The novel part of this paper is a detailed computational analysis of the influence of a WLE on cavitation and noise generation. This complements an experimental study reported by Johari (2015 who gave a qualitative description of the influence of geometry on the location and size of cavitation.

Cavitation modelling is a reasonably mature area and they tend to treat cavitation as a two-phase flow that consists of a liquid and vapour state. Most cavitation models applied to flows around hydrofoils and propellers use the Schnerr and Sauer (2001) model for the growth and collapse of the local cavitation bubbles. For capturing more accurately the cavitation unsteadiness that is related to the shedding mechanism of cavitation formation structures, Da-Qing Li et al. (2009) modified the turbulent viscosity of the SST k-ω model and used it to predict the steady and unsteady cavitation flows for 2D and 3D hydrofoils. The improved modelling of cavitation can further improve the accuracy in calculating the noise radiated signal of a hydrofoil, therefore, the direct computation of the compressible part of the governing equation would be more appropriate to the model improvement however, the computational requirements for this calculation is still prohibitive (Ianiello et al. 2013). A less computational expensive solution would be to use the acoustic analogies where the radiate noise sources can be calculated for an incompressible flow. The model that was first presented by Ffowcs-Williams and Hawkings (1969) (FW-H) can model the monopole noise that can be generated by the oscillation of bubble volumes and other sources present in the flow, the dipole noise that is generated by the loading of a blade and the quadrupole noise that is generated by the turbulence in the flow and high speed flow effects (shock-waves). Seol et al. (2005), Salvatore et al. (2002) and Lidtke et al. (2015) used the FW-H formulation to calculate the generation of noise from ship propellers proving that the FW-H formulation can be a reliable computational tool that can offer good results and in short computational times in particular for the monopole and dipole noise.

The work that is presented in this paper is divided in four sections. Section 2 highlights the scope of this work. In Section 3, the numerical method and computational geometry are described. The hydrofoils are chosen to be NACA 63_4-021 with different amplitude characteristics but with the same wave length. The complex flow mechanisms associated with the presence of the tubercle are compared and explained with a NACA 63_4-021. In the same section the influence of the leading edge on cavitation and the formation of cavity structures are compared with the baseline hydrofoil. Also in section 3 the FW-H formulation that is implemented in ANSYS FLUENT is applied and the effect of the leading edge to cavitation noise are analysed for the hydrofoils studied. Finally section 4 presents the Conclusion and the future work that need to be further completed.

2 SCOPE OF CALCULATIONS

The purpose of this paper is to analyze the influence of WLE on cavitation and the influence of cavitation as a source on the generated sound.

Three different hydrofoils were studied and are referred as the Baseline, 8S and 8L. The hydrofoils were tested for an angle of attack $\alpha = 21^o$ and for a cavitation number $\sigma = 1$, values similar to the experimental study used by Johari (2015). The aim of these calculations were to give a better understanding on how these three hydrofoils are performing under extreme cavitation conditions and to understand the flow mechanism of the wavy leading edges and their contribution to the generated acoustic pressures calculated at the receivers. Finally the study is trying to evaluate if the hydrofoils with protuberances can be applied for reducing and controlling cavitation noise.

3 NUMERICAL METHODS

The section profile hydrofoil used for the WLE hydrofoils 8L and 8S and the Baseline is the NACA 63_4-021. The amplitude A for the 8S hydrofoil was set to 2.5% of the chord length and the wavelength to 25% and for the 8L hydrofoil the amplitude A was set to 12% of the chord length and the wavelength was kept the same with the 8S hydrofoil. The three hydrofoils are presented in figure 1. The average chord length was set to 102 mm and the span to 100.74 mm. Johari (2008) in his work suggested that the local chord length c_z can be calculated by the following expression (1) as a function of spanwise coordinate z, the amplitude A and the wave length λ:

$$c_z = c + A \sin\left(\frac{2\pi z}{\lambda} - \frac{\pi}{2}\right). \tag{1}$$
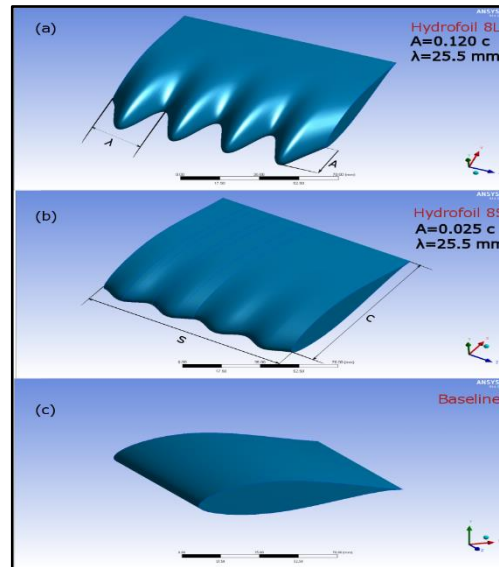

Figure 1: Geometries of the three hydrofoils used for the CFD calculations (a) hydrofoil 8L, (b) hydrofoil 8S, and (c) baseline hydrofoil.

3.1 Geometry and mesh generation

The geometry of the hydrofoils are shown in Table 1. In Table 2 the Boundary conditions for the Baseline hydrofoil are provided.

To demonstrate that the solution is grid size independent , three computational meshes were generated and tested, these three mesh sizes can be seen in Table 3. Figure 2 shows an example of the tetrahedral Grid 3 for the Baseline hydrofoil used in the calculations. The mesh independence study was performed by calculating and comparing the lift coefficient and drag coefficient for an angle of attack of 8°. The differences in the lift and drag coefficients for the Grid2 and Grid3 grid where small however for the rest of the calculation Grid3 was used for the calculations. Similar the same grid independency analysis performed for the 8S and 8L hydrofoils.

Table 1: Basic Geometry characteristics of the modified wavy leading edge hydrofoils

Hydrofoil characteristics	Hydrofoil S	Hydrofoil L	Baseline
Chord (mm)	102	102	102
Amplitude(mm)	$0.025c$	$0.120c$	0
Span (mm)	100.74	100.74	100.74

Table 2: Boundary Conditions for the three hydrofoils

Boundary Condition	Value
Velocity inlet (m/s)	1.83
Turbulence model	$k - \omega$
Turbulent intensity(%)	1
Turbulent viscosity ratio	10
Pressure outlet (Pa)	23600
Hydrofoil wall surface	No-Slip
Side vertical walls	Slip

Table 3: Computational grids used in the CFD simulation

Grid	Cells	CD (AOA=8°)	CL (AOA=8°)
Grid 1	1.82 million	0.17553	0.83419
Grid 2	3.32 million	0.17424	0.81509
Grid 3	4.64 million	0.17525	0.81652

3.2 Cavitation model

In ANSYS Fluent the multi-phase model takes that the working medium consists of two phases: liquid (water) and gas (water vapour). As a result the RANS equations are solved for a mixture fluid with a density ρ, the density can be calculated in the flow cells provided that the volume fractions between the two phases are known.
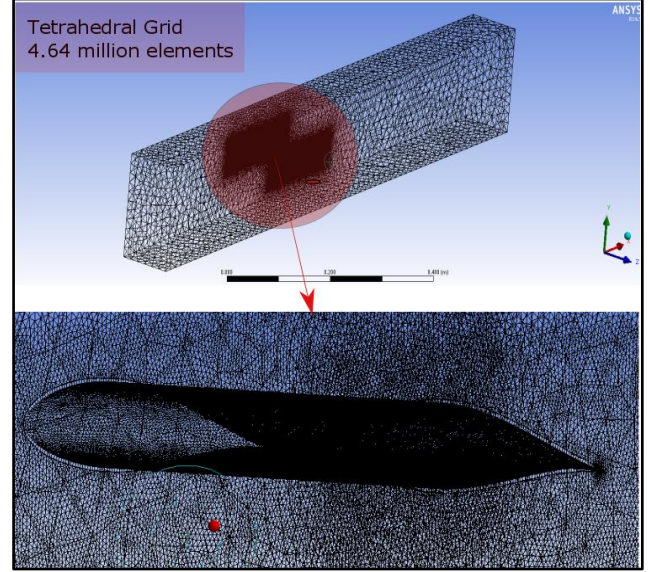

Figure 2: The grid size used for the calculations for the Baseline case hydrofoil.

The volume fraction for the water vapour and water liquid α_v and α_l can be calculated by applying the cavitation model of Schnerr-Sauer (2001). The model solves the vapour volume fraction using the following equation:

$$\frac{\partial}{\partial t}(a_v\rho_v) + \nabla \cdot (\alpha_v\rho_v\boldsymbol{v}_m) = R_e - R_c. \tag{2}$$

where ρ_v is the vapour density; $\boldsymbol{v}_m$ is the mixture velocity. The void fraction grows due to an evaporation source R_e and decreases due to a R_c condensation sink.

The source terms R_e and R_c were derived from the generalized Rayleigh-Plesset equation with the assumption that there is no gas dissolved in the liquid water and therefore only the mass transfer between the vapour and the liquid phases were considered. The closure terms in the right-hand side of (2) are

$$R_e = \frac{\rho_v\rho_l}{\rho_m}\alpha(1-\alpha)\frac{3}{\Re_B}\sqrt{\frac{2}{3}\frac{(p_v-p)}{\rho_l}}. \tag{3}$$

and

$$R_c = \frac{\rho_v\rho_l}{\rho_m}\alpha(1-\alpha)\frac{3}{\Re_B}\sqrt{\frac{2}{3}\frac{(p-p_v)}{\rho_l}}. \tag{4}$$

When the local static pressure (p) is greater than the vapour pressure (p_v) $p > p_v$, $R_e = 0$ while, when $p < p_v$, $R_c = 0$. Here ρ_l, ρ_v are the density of the liquid and vapour. The bubble radius $\Re_B$ is calculated as follows:

$$\Re_B = \left(\frac{\alpha}{1-\alpha}\frac{3}{4\pi}\frac{1}{n_0}\right)^{\frac{1}{3}}. \tag{5}$$

where n_0 is the bubble number density; and the default value used is 10^{13}. The density of the mixture becomes:

$$\rho_m = \rho_v + (1 - \alpha_v)\rho_l. \tag{6}$$

The continuity equation for the mixture flow is:

$$\frac{\partial \rho_m}{\partial t} + \nabla \cdot (\rho_m) = 0. \tag{7}$$

The momentum equation for the mixture is:

$$\frac{\partial}{\partial t}\left(\rho_m \boldsymbol{v}_m\right) + \nabla \cdot (\rho_m\boldsymbol{v}_m\boldsymbol{v}_m)$$

$$=-\nabla p+\nabla\left[\mu_m(\nabla\mathbf{v_m}+\nabla\mathbf{v_m^T})\right]+\rho_m\vec{g}+\vec{F}. \qquad (8)$$

The initiation of cavitation is characterised by the ratio of static pressure (above vapour pressure) to the dynamic pressure component. This local measure – the cavitation number σ - is defined as:

$$\sigma=\frac{2(p-p_v)}{\rho|v_m|^2}. \qquad (9)$$

The time step for the unsteady RANS simulation was set to 5 e^{-4} s and for 400 iterations.

3.3 Turbulence model

Cavitation flows are non-Boussinesq and compressible so that the turbulence in the vapour phase has a weak influence on the overall dynamics. The dynamics are largely controlled by the changing inertia of the fluid mixture, and turbulence and vorticity generated at the walls. The process of wake generation and cavitation in low pressure regions is an unsteady process. The turbulence model chosen to close the Reynolds stress terms in (8) was the modified SST $k-\omega$ model which is a two-equation closure which incorporates compressible effects. This is a well-known model which has been tested for unsteady cavitation past two-dimensional and three-dimensional hydrofoils Da-Qing Li (2009). Turbulent viscosity is considered to be reduced due to the compressibility effects in the local mixture-phase, this also results to a decrease of the turbulence levels and Reynolds stresses. The modified SST $k-\omega$ model allows the capturing of phenomena like the shedding of cavitation vortices from the hydrofoil and the re-entrant jet that is responsible for the detachment of the cavitation bubbles that are attached to the hydrofoil surface. Following Coutier-Delgosha et al. (2003), the turbulent viscosity is modified (as compared to the standard SST model) using a UDF to control the sharpness of viscous stresses across the smeared vapour-liquid interface. The turbulent dynamic viscosity is modified as

$$\mu_t = \left(\rho_v + \frac{(\rho_m-\rho_v)^n}{(\rho_l-\rho_v)^{n-1}}\right)C_\omega\frac{k}{\omega}. \qquad (10)$$

The function $f(\rho)$ reduces the turbulent viscosity in the regions where the volume fraction of the vapour is high, whereas in areas where the volume fraction of water is higher, the equation takes its initial form. The exponent n has been set 10 by Coutier-Delgosha et al. (2003).

3.4 Hydroacoustic model

FLUENT uses the Ffowcs Williams-Hawking's (FW-H) equation for the prediction of mid and far field noise. This method is based on Lighthill's acoustic analogy and is less computational demanding than the direct acoustic simulation technique. For obtaining a solution by applying this integral approach, the flow field has to be obtained by using the appropriate governing equations such as unsteady RANS equations, DES, LES or BEM methods. The flow field results contain the major noise sources that are used to solve the wave equation and determine the sound at the receivers. The FW-H equation is a linearized wave equation that describes the far field acoustic pressure component. The source terms on the right-hand side are generated by viscous, inertial and pressure stresses acting on surfaces or volumes.

$$\frac{1}{a_0^2}\frac{\partial^2 p'}{\partial t^2} - \nabla^2 p' =$$
$$\frac{\partial^2}{\partial x_i \partial x_j}\{T_{ij}H(f)\}$$
$$-\frac{\partial}{\partial x_i}\{[P_{ij}n_j + \rho u_i(u_n-v_n)\delta(f)\}$$
$$+\frac{\partial}{\partial t}\{[\rho_0 u_n + \rho(u_n-v_n)]\delta(f)\}, \qquad (11)$$

where, a_o = velocity of sound; p' = sound pressure at far field u_i = fluid velocity component in the x_i direction; u_n = fluid velocity component normal to the surface $f = 0$; v_i = surface velocity component in the x_i direction; v_n = surface velocity component normal to the surface. T_{ij} = is the Lighthill stress tensor given by (12); P_{ij} = is the compressive stress tensor given by (13).

$$T_{ij} = \rho u_i u_j + P_{ij} - a_0(\rho-\rho_0)\delta_{ij}. \qquad (12)$$

$$P_{ij} = p\delta_{ij} - \mu\left(\frac{\partial u_i}{\partial x_j} + \frac{\partial u_j}{\partial x_i} - \frac{2}{3}\frac{\partial u_k}{\partial x_k}\delta_{ij}\right). \qquad (13)$$

Here $f = 0$ denotes a mathematical surface that is introduced to surround the exterior flow domain, where $f > 0$ the space is unbound and the use of the generalized function theory with the Green function can be applied to obtain the solution. The surface ($f = 0$) can be considered as the source surface or emission surface. This surface can be placed and coincide with a body in the flow domain or to be a permeable surface away from the body surface. The forcing terms are weighted against $\delta(f) = $ Dirac delta function; $H(f) = $ Heaviside function which represent a surface. From (11) it is apparent that three different source terms exist, two linear sources which are the surface sources representing the contributions from the monopole and dipole acoustics sources and one non-linear source which is the volume source (quadrupole sources). The last source takes into account all other sources acting away from the surface $f = 0$. If this surface matches with the body surface S, the not permeability condition $u_n = v_n$ results to a more simplified version of (11) and with the use of Green's function takes the following form:

$$4\pi p'_T(\boldsymbol{x},t) = \frac{\partial}{\partial t}\int_{f=0}\left[\frac{\rho_0 v_n}{r|1-M_r|}\right]_\tau dS \quad. \qquad (14)$$

$$4\pi p'_L(\boldsymbol{x},t) = \frac{1}{c_0}\frac{\partial}{\partial t}\int_{f=0}\left[\frac{p'\,\hat{n}\cdot\hat{r}}{r|1-M_r|}\right]_\tau dS + $$
$$\int_{f=0}\left[\frac{p'\hat{n}\cdot\hat{r}}{r^2|1-M_r|}\right]_\tau dS\,. \qquad (15)$$

where, r is the distance of the receiver from the source; $\hat{n},\hat{r}$ = are the normal (to the surface f) and the radiation vector respectively; M_r = Mach number in the radiation direction, τ = retarded time.

Equations (14) and (15) are the Farassat formulation 1. For the non-linear source term the use of the Green's function results to the following equation:

$$4\pi p'_Q(\boldsymbol{x},t) = \frac{1}{a_0^2}\frac{\partial^2}{\partial t^2}\int_V\left[\frac{T_{rr}}{r|1-M_r|}\right]_\tau dV + $$
$$\frac{1}{a_0}\frac{\partial}{\partial t}\int_V\left[\frac{3T_{rr}-T_{ii}}{r^2|1-M_r|}\right]_\tau dV + \int_V\left[\frac{3T_{rr}-T_{ii}}{r^3|1-M_r|}\right]_\tau dV. \qquad (16)$$

The contribution of (16) is considered to be small in subsonic flows and therefore FLUENT disregards this source. Thus the remaining sound sources are consisting only from monopole and the dipole:

$$p'(\boldsymbol{x},t) = p_T'(\boldsymbol{x},t) + p_L'(\boldsymbol{x},t). \qquad (17)$$

The solution of the FW-H equation provided by FLUENT is based on a boundary integral method which requires identity source and sinks on an interior boundary and external surface (that lies within the computational domain). The outer surface must be taken to be large enough that all the sound sources in the flow interior are included. The forcing terms are slightly modified to account for the significant change in the fluid density (from vapour to liquid) and the FLUENT strategy follows that of Di Francescantonio (1997), by assuming that:

$$U_i = \left(1 - \frac{\rho}{\rho_0}\right)v_i + \frac{\rho}{\rho_0}u_i \ . \qquad (18)$$

$$L_i = P_{ij}\hat{n}_j + \rho u_i(u_n - v_n) \ . \qquad (19)$$

Therefore the solution to (11) is given by the following expression:

$$4\pi p_T'(\boldsymbol{x},t) = \frac{\partial}{\partial t}\int_{f=0}\left[\frac{\rho_0(\dot{U}_n+U_{\dot{n}})}{r(1-M_r)^2}\right]_\tau dS +$$
$$\int_{f=0}\left[\frac{\rho_0 U_n\{r\dot{M}_r+c_0(M_r-M^2)\}}{r^2(1-M_r)^3}\right]_\tau dS. \qquad (20)$$

$$4\pi p_L'(\boldsymbol{x},t) = \frac{1}{c_0}\int_{f=0}\left[\frac{\dot{L}_r}{r(1-M_r)^2}\right]dS +$$
$$\int_{f=0}\left[\frac{L_r-L_M}{r^2(1-M_r)^2}\right]dS +$$
$$\frac{1}{c_0}\int_{f=0}\left[\frac{L_r\{r\dot{M}_r+c_0(M_r-M^2)\}}{r^2(1-M_r)^3}\right]. \qquad (21)$$

where, $L_r = \boldsymbol{L} \cdot \hat{\boldsymbol{r}}; U_n = \boldsymbol{U} \cdot \hat{\boldsymbol{n}}$. In FLUENT the source surfaces are stationary which results that, $u_i = u_n = U_{\dot{n}} = L_M = M = M_r = \dot{M}_r = 0$. The porous formulation is a suitable post processing method and very effective in providing a solution for the FW-H equation. However this method requires that accurate data are transferred from the hydrodynamic problem to the integration surface, therefore, it is important that the flow field around a body has to be resolved accurately. The use of the unsteady RANS model combined with a modified SST $k - \omega$ turbulence model were successfully tested and experimentally validated in flows around hydrofoils where the flow field needed to be accurately captured therefore, this model can be applied for calculating the flow field around the hydrofoils.

In the hydro-acoustic model studied, three receivers were positioned, at an upstream position, at a position above the leading edge of the hydrofoils and at the downstream position. The integrated surfaces for evaluating the FW-H acoustic pressures are presented in figure 3 and are located at the lower and upper computational boundary walls which are part of the fluid domain.

The FW-H formulation can be used for including the flow, the bubble contribution and the moving boundary contribution. However the simplified application of the FW-H as it is used in Fluent, cannot evaluate at the same time the monopole contribution of the generated moving cavitation volume formations. The complexities of the two model approach are many and cannot be easily resolved

and evaluated. Therefore the interaction of these models (Cavitation model and the FW-H model) needs to be further clarified for defining the appropriate interface that could be better applied for resolving the monopole contribution of noise. Therefore at this study a straightforward approach was applied based to the single bubble model that can be used to evaluate the monopole contribution of the cavitation volume to the far field by applying equation (21). To calculate the acoustic pressure the second time derivative of the cavitation volume needs to be calculated. This information can be extracted by using the cavitation model in Fluent that can provide the average data of the fluctuating cavitation volume fraction. Since the overall volume of the flow domain is known, the average volume of the cavitation formations can be calculated in each time step. The oscillation of the cavitation volume is a monopole noise source which can be radiated uniformly to all directions. By combining the spherical wave equation and the pressure that is estimated from the generalized Bernoulli equation the estimated acoustic pressure is:

$$p'(r,t) = \frac{\rho_0}{4\pi r}\ddot{V}(t - \frac{r}{c_0}). \qquad (21)$$

where, $r =$ distance between source and observer; $\rho_0 =$ fluid density $\ddot{V} =$ second time derivative of the cavitation volume structure.
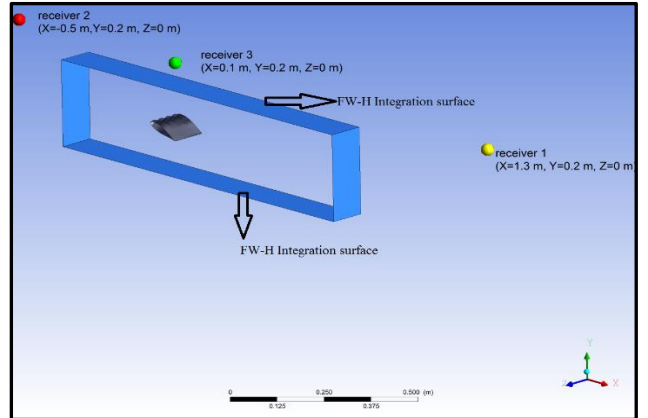

Figure 3: Position of the receivers and the FW-H integration surfaces.

4 RESULTS AND DISCUSSION

4.1 Flow dynamics and the Cavitation formation structures

The results presented in this section are highlighting the differences between the hydrofoils studied and evaluating the effect that the tubercles have to the flow, to the cavitation formation and to the generated noise. In figure 4 the pressure distribution in the spanwise direction is presented for an angle of attack of $\alpha = 21^o$ and a cavitation number of $\sigma = 1$. The difference in pressure distribution between the crests and troughs is affected by the size of the tubercles which seems to induce higher strain to the flow that can lead to the differential motion of the vortices outside the boundary layer. These vortices can reduce the vorticity shedding in the trailing edge changing the sign of the vorticity. In order to visualize this effect, the streamwise vorticity (vorticity x) is presented in figure 5

for the same angle of attack and cavitation number. For the Baseline hydrofoil it can be noticed that half of the hydrofoil is stalled, however for the WLE hydrofoils the flow is partially attached and a strong recirculation region can be observed in the area between the trailing edge and the area downstream the tubercles. Furthermore, the wake characteristics are different for the three hydrofoils and the amplitude of the tubercles seems to affect the wake of the hydrofoils, as a result, the wake of hydrofoil 8L has an increased streamwise vorticity.

In order to investigate the effect of the flow dynamics to cavitation the time sequences of the vapour fraction volumes are presented in figure 6. As it can be noticed cavitation is initially formed near the trough of the hydrofoil, the vorticity stretching mechanism becomes significant in the region of the trough resulting to the fast shedding of cavitation that is gradually swept away from this region by the flow. As it can be noticed the topology of the cavitation for the 8S is different compared to the Baseline hydrofoil and additional the cavitation cycle is affected by the different recirculation characteristics of the flow for these hydrofoils, similar results were presented experimentally by Johari (2015).
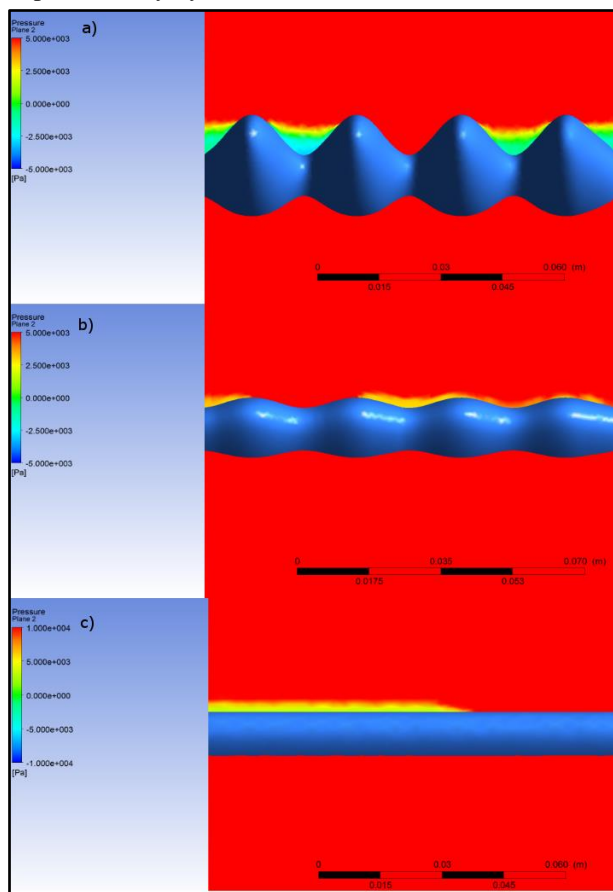

Figure 4: Streamwise vorticity contour at the mid-spanwise position and for an angle of attack $\alpha = 21^o$ and a cavitation number $\sigma = 1$ of a) 8L hydrofoil, b) 8S hydrofoil and c) Baseline hydrofoil.

The time sequences presented in figure 6 can related to the results presented in figure 7 for the lift coefficient. The

formation of cavitation has an effect to the angle of attack of the hydrofoils and is resulting to the change of the lift coefficient. As it can be seen from figure 6b) sheet cavitation is formed in both hydrofoils in the leading edges however for the baseline hydrofoil the leading edge sheet cavitation is occupying a bigger area proportional to the chord length, as presented in figure 6c) sheet cavitation tends to remain attached to the hydrofoil for longer period than for the wavy length hydrofoil. As a result of this prolonged attached cavitation to the hydrofoil, the angle of attack remains increased compared to the wavy length hydrofoil and therefore the lift coefficient remains higher for the Baseline hydrofoil. In figure 6d) the cavitation break off from the Baseline hydrofoil and the piled up of the vapour close to the trailing edge results to the sudden reduction of the lift coefficient. For the wavy length hydrofoil the break off and shedding results to the temporarily increase of the lift coefficient.
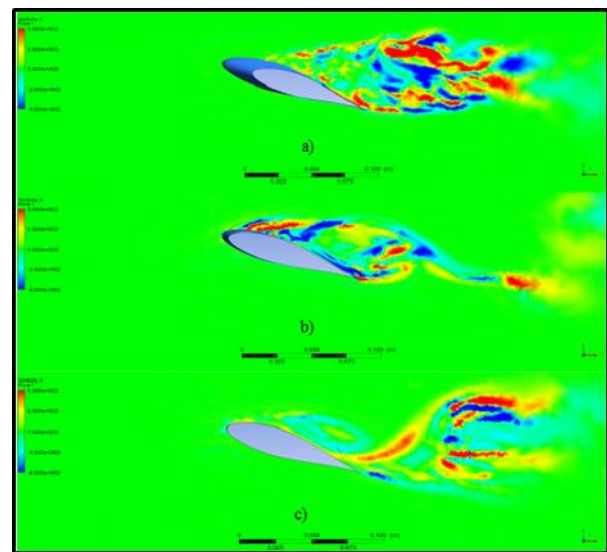

Figure 5: Spanwise pressure distribution contour at 5% chordwise position and for an angle of attack 21° of a) 8L hydrofoil, b) 8S hydrofoil and c) Baseline hydrofoil.

In figure 6e) the effect of the strong streamwise vorticity results to cloud cavitation that is sustained for a longer period in the region above the hydrofoil before it is washed out.

Finally in figure 6f) sheet cavitation starts to be formed in the leading edge and this can result to the increase of the lift coefficient.

The results for the 8L hydrofoil presented in figure 8 are different compared to the baseline and the 8S hydrofoil, the cavitation vapour fraction volumes are significant lower compared to the other two hydrofoils and this was also experimentally observed by Johari (2015). For this case cavitation formation can only be noticed close to the troughs where the local pressure is lower compared to the tubercles region as presented in figure 8a). The main recirculation region that is present in combination with the increased tubercle amplitude results to a flow originated from the pressure surface converging with increased velocity to the central trough drifting away cavitation

volumes that are present in the region. The recirculation generated in the trailing edge has as a result the reduction of the local pressure in this area causing the formation of cavitation near the trailing edge that remains in this area for longer time period before it breaks into smaller cavitation structure formations as a result of the increased recirculation in the trailing edge.
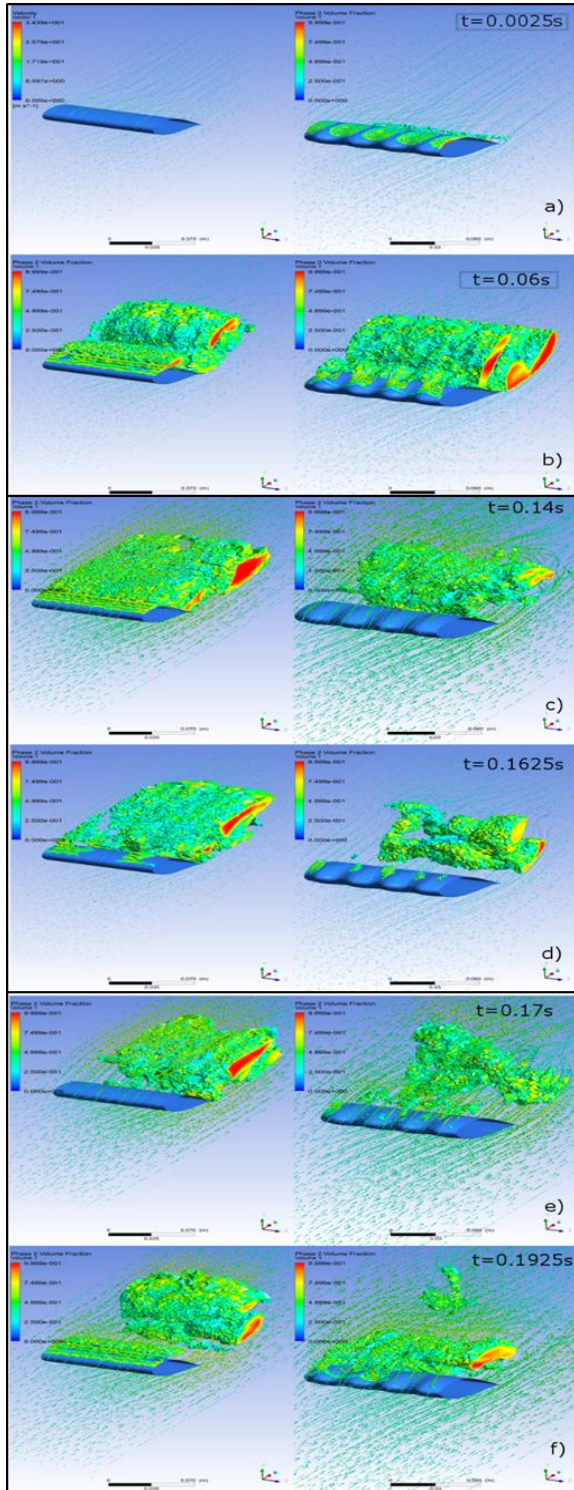

Figure 6: Comparison of the cavitation vapour fraction volumes for the wavy (8S hydrofoil) and baseline leading edge for an angle of attack $\alpha = 21^o$ and a cavitation number $\sigma = 1$.
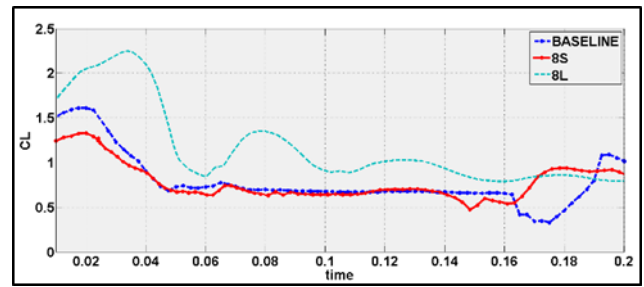

Figure 7: Lift coefficient for the different hydrofoils for of $\alpha = 21^o$ and $\sigma = 1$.

In figure 9 the chordwise pressure coefficient is presented for the wavy leading edge hydrofoils. Figure 9a) shows the pressure coefficient for the 8S and figure 9b) for the 8L. The reference pressure for calculating the pressure coefficient was set to $p_\infty = 20934 \, Pa$ this is the uniform pressure used in the boundary condition in the outlet of the domain corresponding to a cavitation number $\sigma = 1$ for a flow velocity $V_\infty = 6 \, m/s$. The negative values presented in figure 9 indicate pressure reduction below the set pressure, nevertheless the pressure reduction is not always below the vapor pressure. As it was expected the lowest values of the pressure coefficient are developed in the trough cross-section regions and the highest values along the peak cross-section. For the wavy length hydrofoils the pressure distribution in the trough is different for the 8S and the 8L hydrofoil, this has to do with the different positions of the chord length and the differences in the maximum thickness. These differences in magnitude and in the maximum peak positions is resulting to a different spanwise pressure distribution and to a different streamwise vorticity. Furthermore, this variation in the pressure causes a change in the pressure gradient resulting to the compression of the streamwise vortices which are different for the 8L hydrofoil compared to the 8S hydrofoil.

Concerning the over-prediction in the pressure coefficient (higher than one) in figure 9 at the stagnation points is a CFD numerical error that was not possible to be resolved, however it does not influence the explanation provided in relation to the vorticity generation mechanism for these hydrofoils.

3.3 Noise generation

The last part of this work focuses on the evaluation of the generated noise from different hydrofoils. The FW-H formulation was applied in this calculation. Furthermore, the monopole noise source contribution was calculated. In figure 10 the results for the hydrofoils are presented. The FW-H formulation in FLUENT is not calculating the monopole noise sources generated by the fluctuation of the cavitation volume fractions and only the contribution of the generated hydrodynamic noise is taken into account. Therefore, the contribution of the wake for the WLE hydrofoils seems to generate a higher acoustic pressure for the applied angle of attack and cavitation number compared to the Baseline hydrofoil. However, the contribution of the monopole noise source due to the fluctuation of the cavitation volume formation is

significant smaller for the 8L hydrofoil compared to the other two hydrofoils. The average overall noise generated by the 8L hydrofoil is smaller than the average noise generated by the Baseline hydrofoil.
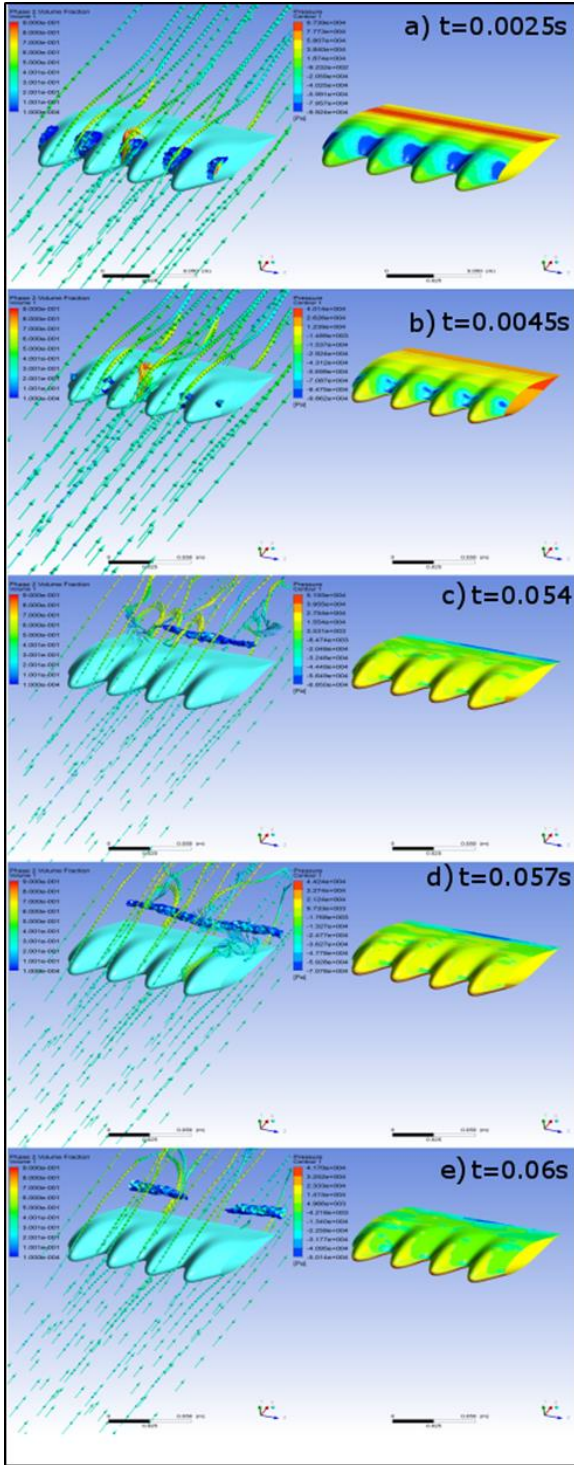

Figure 8: The cavitation vapour fraction volumes and pressure distribution for the 8L hydrofoil for an angle of attack $\alpha = 21^o$ and a cavitation number $\sigma = 1$.
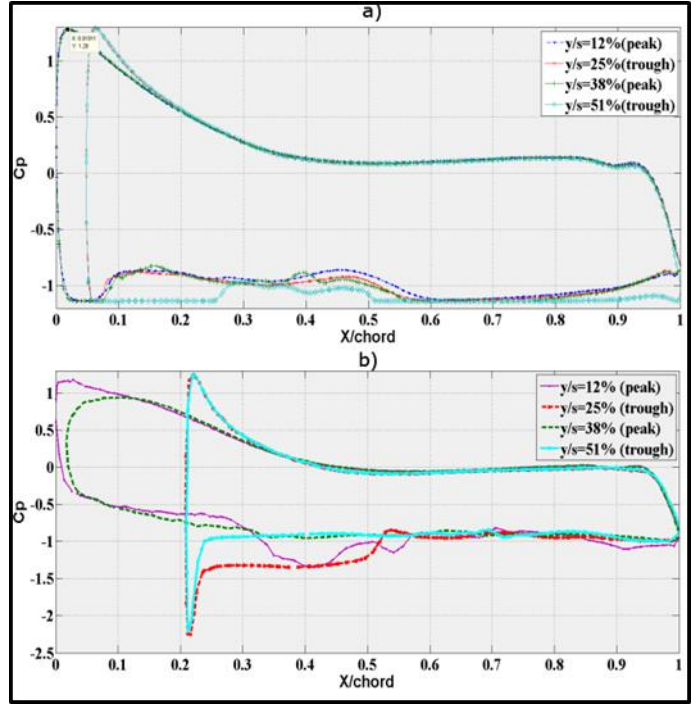

Figure 9: Pressure coefficient ($C_p = \frac{2*(p-p_\infty)}{\rho U_\infty^2}$) for the wavy length hydrofoil at an angle of attack $\alpha = 21^o$ and a cavitation number $\sigma = 1$ a) 8S hydrofoil and b) 8L hydrofoil.
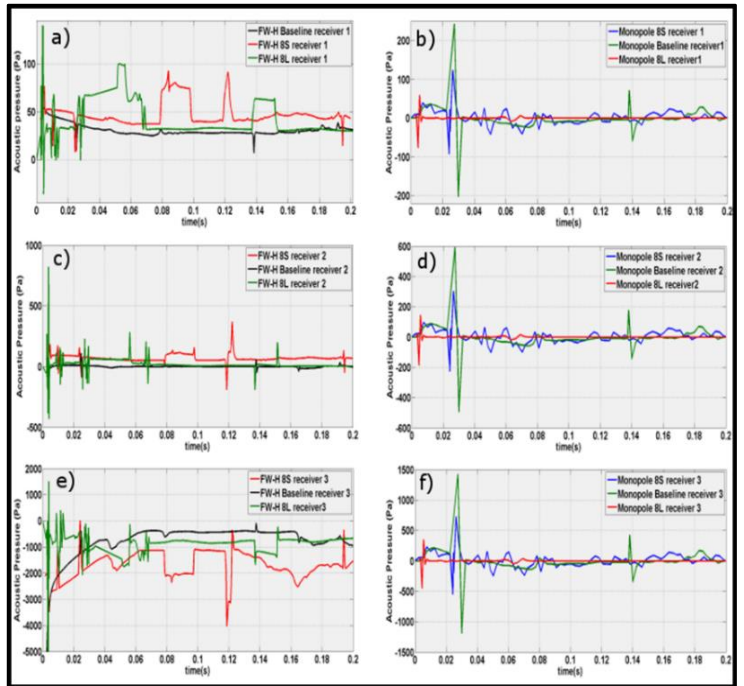

Figure 10: Acoustic pressure calculated with the FW-H formulation and the monopole acoustic pressure due to the cavitation volume fluctuation respectively at a-b) Receiver 1, c-d) Receiver 2 and e-f) Receiver 3.

The results in figure 10 for the monopole acoustic pressure generated by the volume vapour oscillations show that the acoustic pressure peak is at 0.0275 s which is the time the volume acceleration $\ddot{V}$ in 21 reaches its maximum value this can be illustrated also in figure 11 where a direct comparison with the cavitation volume contribution is

provided. The maximum value is physical related to the collapse of the single bubble model. The maximum acoustic pressure is close to the time that the cavitation structure starts to detach from the hydrofoil which is enhanced by the flow recirculation pocket that is present in the mid chord position of the hydrofoil. The pick of the volume fraction acceleration seems to be close to the same period for all three hydrofoils. This is reasonable since the formation and collapse of the overall vapour volume fraction is close. In order to capture the noise contribution from the smaller vapour volume fractions, the volume fractions could be further re-distributed into different sizes and the same analysis could be performed. This analysis would most likely give a different distribution of acoustic pressure for the same time frame than the one that is presented in figure 10.
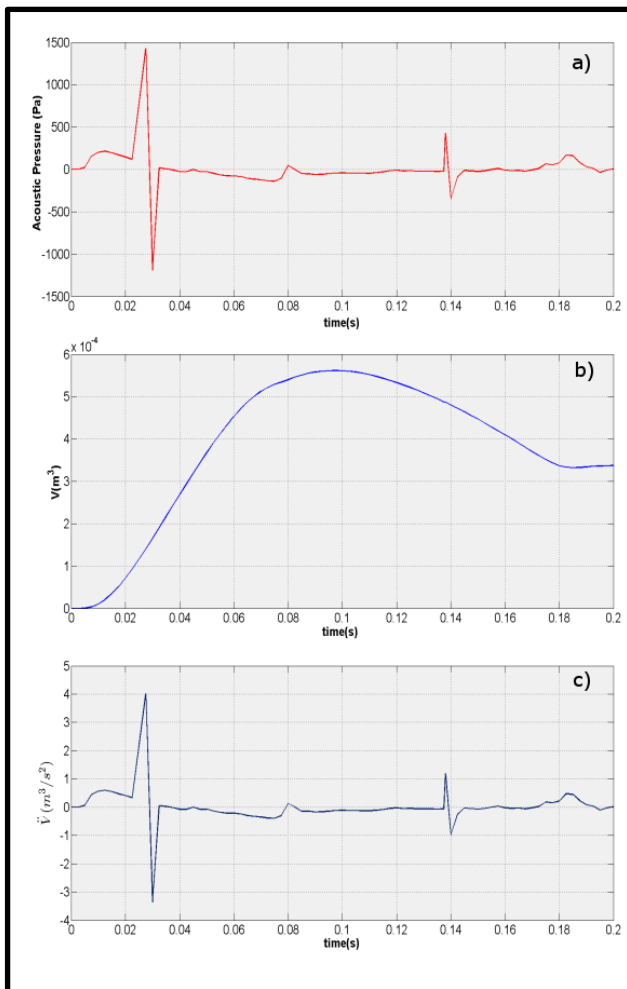

Figure 11: a) The monopole acoustic pressure distribution, b) Cavitation volume distribution, c) Cavitation volume acceleration distribution.

4 CONCLUSIONS AND FUTURE WORK

In this paper we have studied the effect of tubercle size of a WLE hydrofoil on its potential to generate cavitation. We have analyzed the hydrodynamics by combining a CFD cavitation model with an unsteady turbulence model, with slight modifications to sharpen the viscous stresses near the vapour/liquid interface.

The cavitation characteristics for the WLE hydrofoils were found to be quite different compared to the baseline hydrofoil. The streamwise vorticity is affected by the tubercles and it has been found to contribute to the frequency of shedding and break off of the sheet cavitation and to redistribute the positioning of the vapour structures around the hydrofoils. Cloud cavitation was present in the transient calculations of the 8S hydrofoil, however, there were no signs of significant cavitation structures for the 8L hydrofoil. The physical explanation is that large amplitude tubercles generate a larger secondary flow that consists of streamwise vorticity. The streamwise vorticity tends to destabilise the wake so that a cavitation bubble cannot grow behind the leading edge.

The FW-H formulation certainly accounts for the production of sound due to rigid surfaces and the sound generated internally within the fluid. We have applied the standard FW-H formulation in FLUENT to calculate the hydrodynamics noise. The results suggest, in contrast to our expectations, that the FLUENT predicted far field sound is increased in amplitude as compared to the baseline hydrofoil. To analyze this further we estimated the far field sound due to the variation of rate of change of the total vapour volume as a function of time, since this gives the far field sound monopole. This shows that the sound contribution from the cavitation is decreased as compared to the baseline hydrofoil.

The first major scientific challenge for the future is how to correctly incorporate FH-W models into commercial codes so that the noise generated by the flow and cavitation can be correctly identified and evaluated. The second major challenge is how to exploit this type of geometry in future propeller design.

REFERENCES

ANSYS, (2014). 'Solver Theory Guide FLUENT 14.5'. ANSYS-FLUENT, Pennsylvania', USA.

Coutier-Delgosha, O., & Reboud, J.L., Delannoy, Y. (2003). 'Numerical simulation of the unsteady behaviour of cavitating flows', Int.J. Numer. Meth. Fluids 2003; **42**:527–548.

Custodio, D. (2007). 'The effect of Humpback Whale-Like Leading Edge Protuberances on Hydrofoil Performance'. Worcester Polytechnic Institute, Worcester-Massachusetts, USA.

Da-Qing Li, Grekula, M., & Lindell, P. (2009). 'A modified SST k-ω Turbulence Model to Predict the Steady and Unsteady Sheet Cavitation on 2D and 3D Hydrofoils'. Proceedings of the 7th International Symposium on Cavitation CAV2009, Ann-Arbor, Michigan, USA.

Di Francescantonio, P. (1997). 'A new boundary integral formulation for the prediction of sound radiation'. J. of Sound and Vibration, **202(4)**, pp.491–509.

Ffowcs Williams J.E., & Hawkings D.L. (1969). 'Sound generation by turbulence and surfaces arbitrary motion'. Philos Trans R Soc, **264(A1151),** pp.321-342.

Hansen, K. L., Rostamzadeh N., Kelso R.M., & Dally B.B. (2016). 'Evolution of the streamwise vortic s generated between leading edge tubercles', J. Fluid Mech., **vol.788**, pp.730-766, Cambridge University Press 2016.

Ianniello, S., Muscari, R., & Di Mascio, A. (2013). 'Ship underwater noise assessment by the acoustic analogy. Part I: nonlinear analysis of a marine propeller in a uniform flow'. J. Marine Science Technology, **18** pp.547-570.

International Maritime Organization (2014). 'Guidelines for the reduction of underwater noise from commercial shipping to address impacts on marine life'. MEPC.1/Circ833, London, UK.

Johari, H., Henoch, C. W., Custodio, D. & Levshin, A. (2007), 'Effects of leading-edge protuberances on airfoil performance'. AIAA J., **45**, 2634–2642

Johari, H. (2008). 'Applications of Hydrofoils with leading Edge Protuberances'. Final Technical report for Office of Naval Research contract, N00014-08-1-1043, Northridge, USA.

Johari, H. (2015). 'Cavitation on hydrofoils with sinusoidal leading edge'. 9th International Symposium on Cavitation (CAV2015) Journal of Physics:, **656** (2015) 012155.

Lidtke, A.K., Turnock, S.R., & Humphrey V.F. (2015). 'Use of Acoustic Analogy for Marine Propeller Noise characterization'. Fourth International Symposium on Marine Propulsors smp15, Austin, Texas, USA.

Miklosovic, D.S., Murray, M.M., Howle, L.E., & Fish, F. (2004). 'Leading-Edge tubercles delay stall on humpback whale (Megaptera novaeangliae) flippers.' Phys. Fluids, **16,** L39.

Salvatore, F. & Ianniello, S. (2002). 'Preliminary results on acoustic modelling of cavitating propellers'. IABEM 2002, International Association for Boundary Elements Methods, Austin, TX, USA.

Sauer, J. & Schnerr, G.H. (2001). 'Development of a new cavitation model based on bubble dynamics'. Journal of Applied Mathematics and Mechanics, vol.**81**, pp.561-562.

Seol, H., Suh, J.C., & Lee, S. (2005). 'Development of a hybrid method for the prediction of underwater propeller noise'. Journal of Sound and Vibration, vol. **288**, pp.345-360.